Braking Torque Analysis of Stator Field-Excited Synchronous Machine

Mostafa Fereydoonian
Elmore Family School of Electrical and Computer Engineering
Purdue University
West Lafayette, IN, USA
mostafaf@purdue.edu

Hyunwoo Kim
Elmore Family School of Electrical and Computer Engineering
Purdue University
West Lafayette, IN, USA
kim4852@purdue.edu

Woongkul Lee
Elmore Family School of Electrical and Computer Engineering
Purdue University
West Lafayette, IN, USA
wklee@purdue.edu

***Abstract*—This paper investigates the cross-coupling phenomenon in stator field-excited synchronous machines. Due to armature reaction, the excitation magnetic field is dragged away from the d-axis by the armature magnetic field, resulting in the presence of cross-coupling inductance L_{dq}. Furthermore, the excitation field itself experiences cross-coupling effects—meaning that, in addition to the mutual inductance L_{df} between the d-axis and the excitation field, another mutual inductance component L_{qf} exists between the q-axis and the excitation field. Neglecting these terms can result in significant errors in torque calculation. In this work, analytical expressions for the cross-coupling inductance L_{dq} and the mutual inductance L_{qf} are derived. The FEA-based frozen permeability method is employed to accurately determine these inductance components. The inductances were quantified using FEA and the revised mathematical model. The FE-based torque prediction is in excellent agreement with the result of the updated mathematical model, validating the approach.**

***Index Terms*--Braking torque, cross coupling, externally excited synchronous machine, flux-switching machine, high-power density.**

I. Introduction

High torque density remains one of the most critical performance targets in electric machine design, making permanent magnet synchronous machines (PMSMs) the preferred choice in many traction applications. However, growing concerns over the cost, sustainability, and geopolitical risks associated with rare-earth (RE) materials have driven both industry and governmental agencies to seek alternative motor technologies [1]-[3]. Among these, externally excited synchronous machines (EESMs) have emerged as a promising candidate. By replacing RE magnets with electromagnetically excited rotor windings, EESMs offer several advantages, including adjustable magnetic field excitation. This controllability enables higher efficiency under high-speed operating conditions and improved adaptability across a broad operating range. Such characteristics make EESMs particularly attractive for long-distance and high-speed driving scenarios, where their efficiency can exceed that of PMSMs. As of 2020, about 77% of propulsion motors in hybrid and battery electric vehicles were PMSMs, while magnet-free induction machines and EESMs accounted for approximately 17% and 6%, respectively [4]. Recently, an increasing number of automakers and suppliers have intensified their research and development efforts toward advancing EESM topologies [2], [3].

Although EESM technology offers several advantages, it also presents notable challenges. A key issue is the requirement for electrical power transfer to the rotor, traditionally achieved using slip rings and brushes. These components are prone to wear, sparking, and dust generation, which can limit power density and maximum operating speed due to mechanical vibrations. Over the past two decades, advancements in power electronics and wireless power transfer have facilitated the development of brushless exciters for EESMs, effectively mitigating these limitations [5]. The two most widely adopted wireless power transfer techniques are rotary transformers and rotary capacitors. However, these methods exhibit inferior dynamic performance, restrict access to rotor windings for measurement and protection purposes, and tend to increase system cost [5]. Moreover, the additional excitation circuitry introduces extra losses, leading to slightly lower overall efficiency compared to permanent magnet machines. EESMs also typically require a larger installation space to accommodate the excitation hardware [5].

Stator field-excited synchronous machines (SFESM) represent a distinctive subclass of EESMs, in which both the field and armature windings are positioned on the stator [6], [7]. This arrangement eliminates the need for brushes and slip rings, resulting in a more robust and reliable system. SFESMs offer several advantages, including a robust rotor structure similar to a switched reluctance machine, low cost, effective thermal management, concentrated winding, fault tolerance, and flux regulation [6], [7]. The co-location of both field and armature windings in the stator enhances heat dissipation, enabling higher allowable current densities and consequently greater torque density.

However, coexistence of both field and armature windings on one side of the machine's airgap-on the stator, limits the available slot space and increases mutual inductance among the

979-8-3315-8138-1

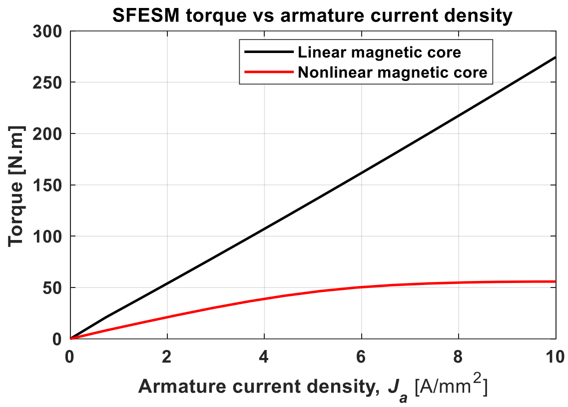

Figure 1. SFESM average torque vs armature current density for ideal linear and nonlinear magnetic core.

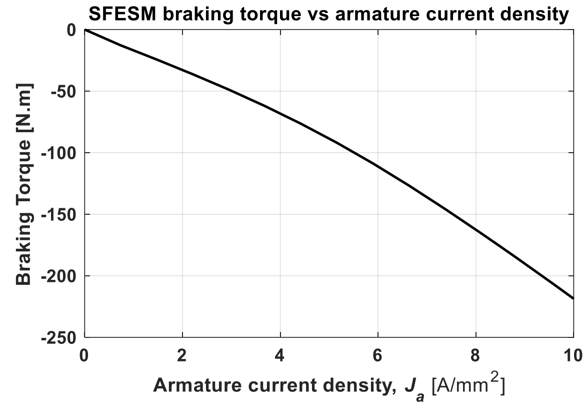

Figure 2. SFESM braking torque vs armature current density.

armature phases. At elevated current densities, when the magnetic core operates in the nonlinear region, cross-coupling effects emerge [8], [9]. As a result, further increases in armature current may generate a counteracting or braking torque component, diminish the net torque gain, and limit power density improvements. This phenomenon underscores the need for detailed torque and braking torque analysis in stator field-excited synchronous machines to better understand the underlying torque production mechanisms and to devise strategies for mitigating braking torque—thereby enhancing overall torque and power density for high-performance motor drive applications.

This paper is organized as follows. Section II investigates the output torque under various armature and field current densities to identify the root cause of the braking torque. The torque generation mechanism is analyzed, and analytical expressions for the cross-coupling inductance L_{dq} and the mutual inductance L_{qf} are derived. Section III employs the finite element analysis (FEA)-based frozen permeability method (FPM) to parameterize and measure all inductance components, thereby quantifying the braking torque and the contribution of different torque components. Finally, Section IV presents key findings and concludes the paper with the main takeaways.

II. SFESM Braking Torque Analysis

SFESMs have both the field and armature windings located on the stator. These machines are generally designed to operate in a saturated condition to achieve a high air-gap flux density. As a result, their performance is strongly influenced by nonlinear magnetic behavior and cross-coupling effects. To highlight the impact of magnetic nonlinearity on the electromagnetic performance of SFESMs, the output torque as a function of armature current density is evaluated using FEA for two magnetic core models: an ideal linear core and a realistic nonlinear core. The average output torque versus armature current density is shown in Fig. 1. As the current density increases and the magnetic core enters saturation, the difference between the actual torque (nonlinear core) and the ideal torque (linear core) becomes increasingly pronounced. This difference represents the braking torque, which counteracts the net torque. The braking torque is illustrated in Fig. 2, where its values appear negative because it contributes in the opposite direction to the produced torque.

The torque production mechanism in this type of synchronous machine requires further investigation to clarify the contribution of each winding set and the associated inductances. To this end, a contour plot of torque versus field and armature current densities is obtained and presented in Fig. 3. To evaluate the ideal torque, the SFESM with a linear magnetic core is simulated, while an SFESM with a nonlinear magnetic core is analyzed to determine the actual torque, plotted in Fig. 4. The difference between the actual and ideal torque represents the braking torque, shown in Fig. 5. As the field and armature current densities increase, the magnitude of the braking torque also rises. For a given field current density (J_f), a higher armature current density (J_a) intensifies magnetic saturation, resulting in greater braking torque and degraded electromagnetic performance. In the following subsection, the SFESM is modeled to examine the influence of magnetic core saturation and nonlinearity on key machine parameters, such as self- and mutual inductances, and consequently on the torque.

A. SFESM Modeling

The torque equation can be derived by analyzing the change and storage of magnetic energy, expressed in terms of flux linkages and inductance components. The stored magnetic energy in the coupling field of the SFESM can be evaluated by establishing the armature and field currents while keeping the system static—that is, without any mechanical output [6]. The flux linkages of the SFESM can be expressed as functions of the inductances, which depend on the rotor position θ:

$$\begin{bmatrix}\lambda_u\\ \lambda_v\\ \lambda_w\\ \lambda_f\end{bmatrix}=\begin{bmatrix}L_{uu} & L_{uv} & L_{uw} & L_{uf}\\ L_{vu} & L_{vv} & L_{vw} & L_{vf}\\ L_{wu} & L_{wv} & L_{ww} & L_{wf}\\ L_{fu} & L_{fv} & L_{fw} & L_{ff}\end{bmatrix}\begin{bmatrix}i_u\\ i_v\\ i_w\\ i_f\end{bmatrix} \quad (1)$$

where L_{uu} is the self-inductance, and L_{uv} is the mutual inductance between the windings. The torque expression can be derived by using coenergy:

$$T=\left.\frac{\partial W_m'(i,\theta)}{\partial\theta}\right|_{i=const.} \quad (2)$$

$$T=\frac{1}{2}\sum_n i_n^2\frac{dL_{nn}}{d\theta}+\frac{1}{2}\sum_k\sum_m i_k i_m\frac{dL_{km}}{d\theta}$$
$$K\neq m,\quad m,n,and\ \ k\in\{u,v,w,f\} \quad (3)$$

979-8-3315-8138-1

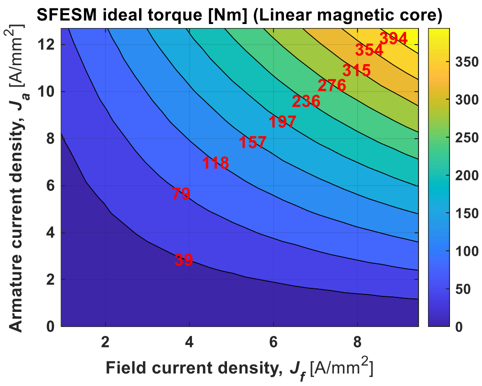

Figure 3. Contour plot of ideal torque of SFESM vs field and armature current densities.

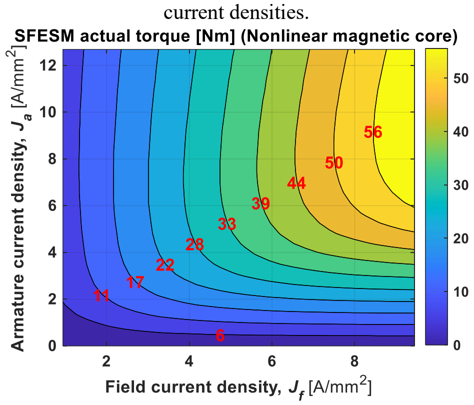

Figure 4. Contour plot of actual torque of SFESM vs field and armature current densities.

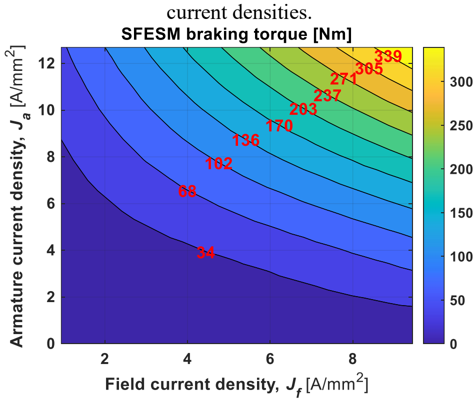

Figure 5. Contour plot of the absolute value of braking torque of SFESM vs field and armature current densities.

By expanding the torque expression for the field and armature windings:

$$T = \left(\frac{1}{2} i_f{}^2 \frac{dL_{ff}}{d\theta} + \frac{1}{2} i_u{}^2 \frac{dL_{uu}}{d\theta} + \frac{1}{2} i_v{}^2 \frac{dL_{vv}}{d\theta} + \frac{1}{2} i_w{}^2 \frac{dL_{ww}}{d\theta}\right) + \left(i_u i_v \frac{dL_{uv}}{d\theta} + i_v i_w \frac{dL_{vw}}{d\theta} + i_w i_u \frac{dL_{wu}}{d\theta}\right) + \left(i_f i_u \frac{dL_{fu}}{d\theta} + i_f i_v \frac{dL_{fv}}{d\theta} + i_f i_w \frac{dL_{fw}}{d\theta}\right) \quad (4)$$

The first four terms on the right-hand side of the torque expression correspond to the torque contributions from the self-inductances of each winding set (L_{ff}, L_{uu}, L_{vv}, and L_{ww}). The next three terms represent the torque components arising from the mutual inductances among the armature windings (L_{uu}, L_{vv}, *and* L_{ww}). The final three terms correspond to the torque contributions from the mutual inductances between the armature and field windings (L_{fu}, L_{fv}, *and* L_{fw}), which are of primary interest in this study. The torque generated by each of these inductance components for a given SFESM is decomposed and summarized in Table I. To highlight the impact of magnetic saturation, the torque decomposition is performed for the SFESM using two types of magnetic cores: an ideal linear core and a nonlinear magnetic core.

TABLE I. SFESM TORQUE GENERATED BY SELF- AND MUTUAL INDUCTANCE FOR LINEAR AND NONLINEAR MAGNETIC CORES (J=8.5 [A/mm^2]).

Linear magnetic core	*f*	*u*	*v*	*w*
f	0.01	74.53	74.28	74.40
u	74.53	-0.04	-0.14	-0.16
v	74.28	-0.14	-0.12	-0.18
w	74.40	-0.16	-0.18	-0.09
Nonlinear magnetic core	***f***	***u***	***v***	***w***
f	-0.02	39.42	39.42	39.47
u	39.42	-7.5	-14.8	-14.8
v	39.42	-14.8	-7.5	-14.8
w	39.47	-14.8	-14.8	-7.5

The terms highlighted in green represent the torque components arising from the mutual inductances between the field and armature windings, all of which have positive values. The terms highlighted in gray correspond to the torque contributions from the self-inductances of the windings. As shown, for a linear magnetic core, these torque components are negligible. However, in the case of a nonlinear magnetic core, the armature winding self-inductances generate approximately –7.5 N.m of torque, which counteracts the net torque. A similar behavior is observed for the armature winding mutual inductances, highlighted in orange. While these components are negligible for the ideal linear magnetic core, they increase significantly—up to around –14.8 N.m—for the nonlinear magnetic core, again opposing the net torque. Therefore, all the terms highlighted in gray and orange act as braking torque components due to their negative values, whereas the green-highlighted terms contribute positively to the overall torque.

B. *SFESM in dq-axis*

The SFESM expressed in the rotor reference frame provides better insight into the effects of magnetic core saturation and nonlinearity. In the dq-axis model, the steady-state voltage equations of the synchronous machine can be expressed as:

$$\begin{aligned} V_d &= R_s i_d + \frac{d\lambda_d}{dt} - \omega_r \lambda_q \\ V_q &= R_s i_q + \frac{d\lambda_q}{dt} + \omega_r \lambda_d \end{aligned} \quad (5)$$

According to classical textbooks:

$$\begin{aligned} \lambda_d &= L_d i_d + L_{df} i_f \\ \lambda_q &= L_q i_q \end{aligned} \quad (6)$$

Substituting (5) and (6) into the torque expression:

$$T = \frac{3}{2} P\left(\lambda_d i_q - \lambda_q i_d\right) \quad (7)$$

$$T = \frac{3}{2} P\left(L_{df} i_f i_q + \left(L_d - L_q\right) i_d i_q\right) \quad (8)$$

979-8-3315-8138-1

However, this classical torque expression cannot fully capture the nonlinear behavior of the SFESM under magnetic saturation. When the SFESM operates under loaded conditions, deep saturation and strong armature reaction significantly affect the inductance prediction, resulting in distinct self- and mutual-inductance components during double excitation. Hence, this classical model remains incomplete. Due to the armature reaction, the excitation field is displaced from the d-axis by the armature magnetic field, giving rise to a cross-coupling inductance L_{dq}. This cross-coupling phenomenon also extends to the excitation field; in addition to the mutual inductance L_{df} between the d-axis and excitation field, another mutual inductance L_{qf} appears between the q-axis and excitation field. Neglecting L_{dq} and L_{qf} leads to torque calculation errors. Therefore, it is essential to consider all inductance components in the flux linkage equations; thus, (6) should be extended to:

$$\begin{aligned}\lambda_d &= L_{dd}i_d + L_{dq}i_q + L_{df}i_f \\ \lambda_q &= L_{qq}i_q + L_{qd}i_d + L_{qf}i_f\end{aligned} \tag{9}$$

Then the torque expression becomes:

$$\begin{aligned}T = \tfrac{3}{2}P\big[&\left(L_{df}i_f i_q - L_{qf}i_f i_d\right) + \\ &\left(L_{dd} - L_{qq}\right)i_q i_d + \left(L_{dq}i_q^2 - L_{qd}i_d^2\right)\big]\end{aligned} \tag{10}$$

The first term on the right-hand side represents the excitation torque, which originates from the mutual inductances between the field and the d- and q-axes (L_{df} and L_{qf}). The second term corresponds to the saliency (reluctance) torque, resulting from the difference between the d- and q-axis inductances. The last term denotes the cross-coupling torque, which arises from the mutual inductance between the d- and q-axes (L_{dq}).

III. Parameter Determination with Frozen Permeability Method

A small-scale SFESM was designed and prototyped for this study. The 2D and 3D views of the machine are shown in Fig. 6. The field winding, shown in orange, is located on the stator in every other slot, while the three-phase armature windings are depicted in red, green, and blue. The machine specifications are summarized in Table II. To investigate the effects of saturation and cross-coupling on the output torque, the finite element analysis (FEA)-based frozen permeability method (FPM) is employed to accurately determine all inductance components. Using FPM, the total flux linkages can be decomposed into contributions from individual current excitations (i.e., I_d or I_q, and or I_f). At a given operating point defined by these currents, a nonlinear FEA simulation is first performed to determine the permeabilities at all nodes of the finite-element mesh. These permeabilities are then "frozen" and used in three linear FEA simulations to compute the d- and q-axis flux linkages (λ_d, λ_q) presented in (9). By freezing the permeabilities, all inductances (i.e., L_{dd}, L_{qq}, L_{df}, L_{qf}, and L_{dq}) can be computed with high accuracy. The overall FPM process is summarized in the flowchart shown in Fig. 7.

To determine the inductances in (9), the following FEA procedure is employed. In the first step, a single nonlinear FEA simulation is performed at the machine's rated operating condition (I_d, I_q, and I_f). After freezing the permeabilities obtained from this simulation, three linear FEA simulations are carried out: in the second step, only I_f is applied while I_d and I_q are set to zero; in the third step, only I_d is applied while I_f and I_q are set to zero; and in the fourth step, only I_q is applied while I_f and I_d are set to zero.

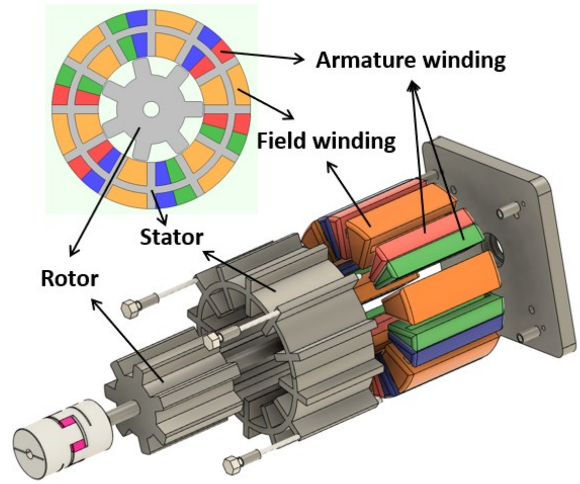

Figure 6. 2D and 3D view of the designed 6S/7R SFESM.

Table II. 6S/7R SFESM Specification.

Parameter	Units	Value
Rated power	W	305
Rated speed	rpm	1000
Rated torque	Nm	2.9
Number of stator-rotor poles	-	6/7
J_a and J_f (armature and field current densities)	A/mm^2	5
N_f (turns per dc coil)	-	200
N_a (turns per coil per phase)	-	100
Stator / Rotor outer diameter	mm	150/78.4
Filling factor	-	0.4
Airgap (l_g)	mm	0.8
Stack length	mm	76.2
Cooling	-	Air cooling

IV. Electromagnetic Performance Comparison

Using (9) and (10) along with the FPM method, the inductance values in the rotor reference frame are predicted. To highlight the effects of magnetic saturation and cross-coupling, this procedure is carried out for two different armature current densities (J_a= 5, and 15 A/mm^2). Table III summarizes all inductance values used in (9) and (10). As the current density increases, L_{df}, which is the primary inductance of interest, decreases from 165.45 to 151.2 µH, while L_{qf}, which is not desirable, increases from 3.3 to 13.76 µH. A higher L_{df} is beneficial because it generates excitation torque arising from the mutual inductance between the field and q-axis. Conversely, the cross-coupling inductance L_{dq}, which negatively affects performance, increases significantly (more than eight times) with higher current density, from –0.93 to –7.99 µH.

The SFESM output torque at rated conditions is evaluated using FEA and calculated using the mathematical model expressed in (9) and (10). The results from FEA are in good agreement with the predictions of the mathematical model (less than 1% error), as summarized in Table IV. The contour plots of magnetic flux density and flux lines for two different current densities are shown in Fig. 8. Higher current densities cause

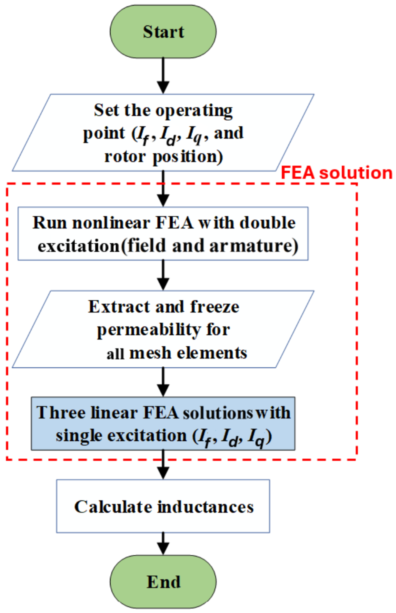

Figure 7. Flowchart for inductance prediction of SFESM with FPM.

TABLE III. SFESM DQ-AXIS INDUCTANCE VALUES FOR DIFFERENT ARMATURE WINDING CURRENTS.

Inductance	Value [μH]	
	J_a=5 [A/mm^2]	J_a=15 [A/mm^2]
L_{dd}	266.9	255.6
L_{qq}	224.59	197
$L_{dq}(=L_{qd})$	-0.93	-7.99
L_{df}	165.45	151.2
L_{qf}	3.3	13.76

TABLE IV. TORQUE COMPARISON OF SFESM EVALUATED BY FEA AND MATHEMATICAL MODEL (@ 1,000 RPM)

Current density [A/mm^2]	J_a= 5 [A/mm^2]		J_a= 15 [A/mm^2]	
SFESM Torque [Nm]	FEA	Mathematical model	FEA	Mathematical model
	3.07	3.066	6.45	6.455
Error [%]	-0.13		0.07	

significant saturation of the stator back iron and teeth. Under elevated current densities, the excitation field is displaced from the d-axis by the armature's magnetic field. The torque components in (10), including excitation, reluctance, and cross-coupling torque, are plotted for the two current densities in Fig. 9. As observed for a higher current density of 15 A/mm², the reluctance and cross-coupling torque curves shift downward, counteracting the excitation torque. These braking torques become more pronounced as the core approaches saturation.

V. CONCLUSION

In stator field-excited synchronous machines, particularly under saturated conditions, the armature current MMF causes the excitation magnetic field to be displaced from the d-axis, which consequently alters the permeance distribution in the rotor and stator cores. The cross-coupling effect rises the L_{qf}, the mutual inductance between the field and q-axis and L_{dq}, the mutual inductance between the d- and q-axis become

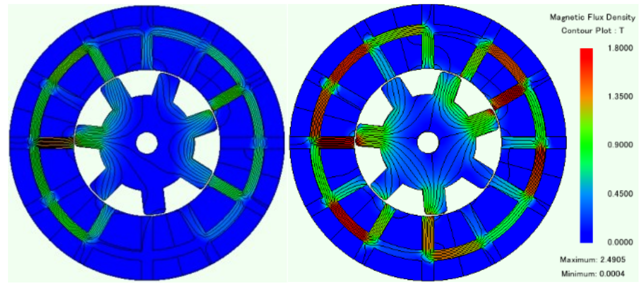

J_a= 5 A/mm^2 J_a= 15 A/mm^2

Figure 8. 6/7 SFESM magnetic flux density contour plot at different current densities (@ 1,000 rpm).

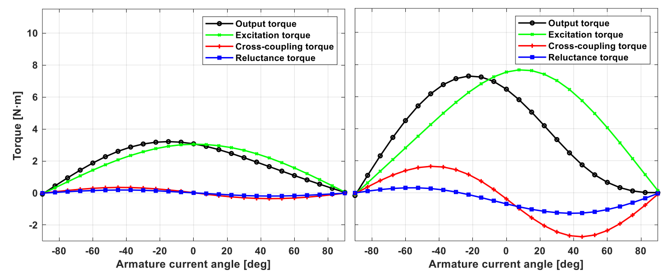

J_a= 5 A/mm^2 J_a= 15 A/mm^2

Figure 9. Torque decomposition of SFESM for different current densities.

significant. Neglecting this effect can result in significant errors in torque calculation. In this paper, the mathematical model of the synchronous machine has been updated to account for all mutual inductances. The inductances were quantified using FEA and the revised mathematical model. The FE-based torque measurements were in excellent agreement with the predictions of the updated model, validating the approach.

REFERENCES

[1] M. Fereydoonian, K. Lee, C. Kiriella, J. Moon and W. Lee, "Closing the Loop on Circular Economy in Transportation Electrification: Reuse, Repurposing, and Recycling of Batteries, Power Electronics, and Electric Machines," in *IEEE Journal of Emerging and Selected Topics in Industrial Electronics*, vol. 6, no. 3, pp. 931-947, July 2025.

[2] "BMW's Magnet-Less Motor: How Does It Work?" MotorTrend, Jan. 13, 2022. https://www.motortrend.com/.

[3] "ZF makes magnet-free electric motor uniquely compact and competitive - ZF," Zf.com, Sep. 2023. https://press.zf.com/press.

[4] "Reduced rare earth and magnet-free motors," *E-Mobility Engineering*, Apr. 25, 2023. https://www.emobility-engineering.com/.

[5] F. Graffeo, Vaschetto, P. Supervisor, Tenconi, and Co-Supervisor, "Modeling and Design of Wound-Field Synchronous Machines for Transportation Applications," 2023.

[6] M. Fereydoonian, D. Bobba and W. Lee, "Multisegment Magnetic Flux Path Analysis of Wound-Field Flux-Switching Machines with Different Winding and Stator-Rotor Combinations," in *IEEE Journal of Emerging and Selected Topics in Industrial Electronics*, vol. 6, no. 3, July 2025.

[7] M. Fereydoonian, K. Lee, D. Bobba and W. Lee, "Comparative Analysis of Wound-Field Flux-Switching Machines with Different Field and Armature Winding Configurations," *2022 IEEE/AIAA (ITEC+EATS)*, Anaheim, CA, USA, 2022.

[8] M. Mabhula and M. J. Kamper, "Computational Efficient Parameter and Performance Prediction of Wound-Rotor Induction Motor," in *IEEE Transactions on Magnetics*, vol. 54, no. 6, pp. 1-7, June 2018.

[9] J. Pang, W. Liu, N. Jiao, J. Wang and P. Ma, "Calculation of Cross-Coupling Inductance and Electromagnetic Torque in Wound-Rotor Synchronous Starter/Generator," in *IEEE Transactions on Industrial Electronics*, vol. 66, no. 7, pp. 5115-5123, July 2019.

979-8-3315-8138-1